HAL
open science

Modelling of a turbulent lean premixed combustor using a Reynolds-averaged Navier–Stokes approach

Alain Coimbra, Luís Fernando Figueira da Silva

To cite this version:

Alain Coimbra, Luís Fernando Figueira da Silva. Modelling of a turbulent lean premixed combustor using a Reynolds-averaged Navier–Stokes approach. Journal of the Brazilian Society of Mechanical Sciences and Engineering, 2020, 42 (5), pp.213. 10.1007/s40430-020-2273-y . hal-03313671

HAL Id: hal-03313671

https://hal.science/hal-03313671v1

Submitted on 22 Jul 2022

HAL is a multi-disciplinary open access archive for the deposit and dissemination of scientific research documents, whether they are published or not. The documents may come from teaching and research institutions in France or abroad, or from public or private research centers.

L'archive ouverte pluridisciplinaire **HAL**, est destinée au dépôt et à la diffusion de documents scientifiques de niveau recherche, publiés ou non, émanant des établissements d'enseignement et de recherche français ou étrangers, des laboratoires publics ou privés.

Noname manuscript No.
(will be inserted by the editor)

Modelling of a turbulent lean-premixed combustor using a Reynolds-Averaged Navier-Stokes approach

Alain P. N. Coimbra · Luís Fernando Figueira da Silva

Received: date / Accepted: date

Abstract This work aims to characterize lean premixed turbulent swirling flames representative of gas turbines and jet engines via a numerical study of flame topologies in a laboratory scale burner. The state of the art of the numerical studies concerning these types of flames is first reviewed, with respect to Reynolds-Averaged Navier-Stokes and Large Eddy Simulations. Then, a turbulent, isothermal flow study is performed within the radial swirler. The impact of mesh refinement levels and boundary conditions on the swirl number and overall flow structure is investigated. The mesh refinement level and slip wall boundary condition alter the computed swirl number significantly. The computed swirl number converges to a value of 0.7, which is larger than the geometrical one, 0.4. Furthermore, using Reynolds-Averaged Navier-Stokes transport equations, closed by the realizable $k - \epsilon$ model, coupled with a two-equation premixed combustion model for methane/air mixtures, two combustion regimes are analyzed. These regimes correspond to the outer recirculation zone flame and an unstable regime. The flow structure is characterized in terms of velocity fields, turbulence and combustion properties. A reaction progress variable comparison is also performed, using existing experimental results, yielding qualitatively similar structures for both studied regimes. Some discrepancies between numerical and experimental results concerning the stable regime may be observed: the computed progress variable at the outer recirculation zone, 0.5, is smaller than the experimental value, 0.8, and the average flame brush thickness, 1 mm, is found to be smaller than the measured, 3 mm.

Keywords Premixed combustion · Turbulent combustion · Swirling flows · Numerical study

Alain P. N. Coimbra
Pontifícia Universidade Católica do Rio de Janeiro
R. Marquês de São Vicente, 225 - 22451-900 - Rio de Janeiro, Brazil
Tel.: +55 21 99769-2865
E-mail: coimbraalain@gmail.com

1 Introduction

Gas turbines are prevalent for aircraft engines and large scale energy generators, due to their relative high efficiency and stability. A configuration adopted for the combustion chamber of such systems is that of turbulent lean premixed flames. The lean premixing of reactants leads to lower burning temperatures, which significantly diminishes the NOx emissions, as well as soot formation. In these configurations, the swirler, a mechanical device that induces a significant amount of tangential momentum to the flow, imposes a turbulent, swirling flow, which aids the flame stabilization and ensures pre-mixing of fuel and air upstream to the flame. This work is devoted to the investigation and understanding of a configuration representative of such combustion systems, as well as to a numerical study regarding turbulent lean premixed, swirl-stabilized premixed combustion.

The numerical studies presented here are the counterpart to the experimental research activities performed at PUC-Rio. In these studies, using two different swirlers and, therefore two different swirl numbers, several flame topologies for methane/air combustion have been observed [26]. For these values of the geometrical swirl number, OH chemiluminescence allowed visualization of different flame topologies, also as a function of methane/air equivalence ratio and volumetric flow rate [23]. A literature review indicates that several lean premixed swirling combustors experiments have been recently addressed. Different combustion regimes and instability characteristics have been observed in turbulent methane/hydrogen/air flames in a swirling flow [31]. Transitions between topologies and their interactions with the combustion chamber walls have been experimentally studied [15], as parameters controlling the shape of swirling flames were identified.

Several numerical studies regarding interactions between turbulence and premixed combustion in swirl-stabilized combustors have also been conducted. Turbulence modelling, and its interactions with chemical reactions have been extensively discussed in the context of time-averaged Navier-Stokes equations [30]. A Reynolds-Averaged Navier-Stokes approach regarding swirl effects on the flame dynamics of a lean premixed combustor has also been recently addressed [22]. The realizable $k-\epsilon$ has been determined to be the most predictive for high swirl numbers, as it has shown best agreement with experimental results. For a critical swirl number, around 0.75, an inner recirculation zone, also referred as vortex breakdown, has been found to arise.

Most recent numerical studies of turbulent, swirling flame dynamics employ large eddy simulations. Indeed, LES is a particularly attractive approach for the study of unstable regimes, where the flow field of concern is unsteady and dominated by turbulent motions that cannot be adequately resolved using classical RANS models. Potential sources that may control the overall quality of LES results for turbulent premixed flames have been recently identified [29]. Chemistry description, flame/turbulence interaction modelling, numerical solving, boundary conditions, wall numerical treatments and wall temperature and heat losses have been pointed out as being crucial. On a partially

premixed swirling combustor, LES have been conducted in order to investigate the mixing of fuel and air in the swirler and burner nozzle that leads to thermoacoustic oscillations [20]. The importance of thermal boundary conditions on the combustor walls for the prediction of instability regimes has also been identified as a relevant issue [19]. Modelling of the burner solid structure has been found to contribute only slightly to changes on the mean velocity field, but to improve the prediction of frequency and amplitude of unstable modes, when compared to experimental results. On a swirl-stabilized methane-air flame, LES have been applied for determining velocity and OH mass fraction profiles in transient blow-off simulations [21]. The flame lift-off height and the local extinction phenomena are used for comparing a flamelet/progress variable model with a thickened flame model. A joint experimental and numerical study has also been conducted regarding a swirl-stabilized cylindrical combustor [24]. Chemiluminescence and dynamic pressure measurements have been used to study thermoacoustic instabilities in a lean premixed methane/air flame. Concerning LES, an Eulerian stochastic field method has been applied to describe turbulence/chemistry interactions. Additionally, using dynamic mode decomposition, unstable flame modes could be investigated, and the azimuthal transport of hot combustion products around the centerline of the combustion chamber analyzed. Using a skeletal chemistry approach coupled to a thickened flame model, LES have been used to study the effects of heat loss in the flame lift-off, which causes transitions of stable flame regimes in premixed swirling flames [3]. The addition of wall heat loss causes the flame transition from a M-shaped flame to a V-shaped flame.

The main objective of this work is to discuss the modeling results of a joint numerical and experimental effort regarding premixed swirling flames in novel swirler and combustion chamber configurations. This burner has been developed in a partnership between PUC-Rio and the CNRS/CentraleSupelec EM2C laboratory. This is the first modeling attempt of this novel swirler configuration and lean premixed combustion chamber. It is thus a stepping stone to studies involving more advanced – and costly – models. To achieve this goal, it is proposed to:

- Perform an isothermal flow study, for mesh verification and boundary condition determination;
- Perform the reactive flow study, in order to characterize the flow field and identify flame topologies;
- Compare regimes limits and characteristics with the corresponding experimental results.

This paper is divided in four sections. The first section presented the motivation, a brief literature review regarding lean premixed combustion studies and the objectives. In the second section, the numerical methodology is given. The computational domain of the studied premixed swirling combustor is explained. Then, the numerical models for turbulence and premixed combustion are briefly discussed. The computational grid, boundary conditions and numerical schemes are addressed. The third section presents the computed results,

regarding an isothermal flow study within the swirler and reactive flow study within the combustion chamber for different combustion regimes. Finally, in the fourth section, the conclusion and perspectives for future works are discussed.

2 Numerical Methodology

In this section, the numerical methodology is presented. The domain of interest associated to the experimental configuration is first exposed, and the computational domain meshing procedure is analyzed. A model description of turbulence and premixed combustion is briefly given, boundary conditions details and difficulties are explained, and the numerical schemes given.

2.1 Computational Domain

Figure 1 shows the developed experimental combustion chamber (left). This chamber consists of 4 vertical quartz windows, which are resistant to high temperatures and transparent to UV radiation, thus allowing for the combustion region visualization. The stainless-steel chamber base is water cooled, which is required due to its contact with high temperature gases [23]. The planar laser induced fluorescence technique has been used to characterize the observed flame regimes. A dye laser system and a CCD camera have been used in the tests [6]. The laser sheet is perpendicular to the camera, and passes through the center of the combustion chamber. To control the air/methane mixture, two flow meters have been used, both with 0.5 % reading plus 0.1 % full scale uncertainty. The interested reader may refer to the corresponding experimental studies in order to gain further insight on the used facility and associated measurement techniques [33],[26],[23].

For the numerical solution, the configuration of interest consists of a radial swirler and the adjoining square-sectioned combustion chamber. As shown in Fig. 1, the combustion chamber is square-sectioned, with a width of $L = 40$ mm. The actual chamber height at the experimental setup is $H_c = 170$ mm, but it has been reduced to $H_c = 100$ mm in this work due to computational resources limitations. A pyramid-shaped convergent structure is placed at the top of the combustion chamber, which provokes a flow acceleration at the domain outlet. The top structure has a height of $H_p = 15$ mm and the outlet has a width of $L_p = 10$ mm. This structure is a modelling artefact which diverges from the experimental counterpart of this work. Indeed, the acceleration of the flow near the domain outlet has proven to prevent the occurrence of reverse flow, which interferes with the converging process of the numerical solution.

The swirler, which is coupled at the base of the combustion chamber, is denominated SW06I [23]. The overall design, inlet and outlet sections are presented in Fig. 2. The bluff body main function is to provide for the flame anchoring near the combustion chamber base. It may be seen from Fig. 2(a)

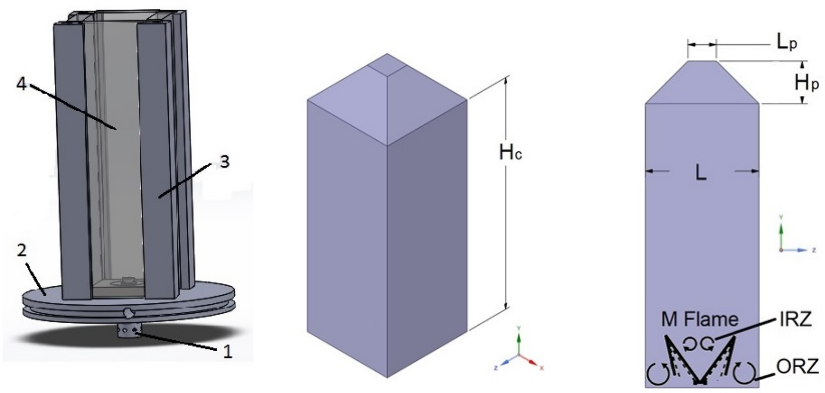

(a) Experimental configuration.

(b) Isometric view.

(c) Frontal view.

Fig. 1 Combustion chamber schematic view. In the experimental configuration: 1 swirler, 2 cooling base, 3 confinement, 4 quartz window, adapted from [26].

that the SW06I has the bluff body surface flushed to the surface of the swirler exit. Fig. 2(b) shows the swirler inlet section, where it may be observed that the mixture is fed tangentially to the chamber. In this particular swirler, six air/fuel inlets, with identical diameters, are radially distributed at the device's base. The swirler exit section is depicted in Fig. 2(c). The inverted cone can be perceived at the upper base, narrowing the flow upstream to the expansion at the combustion chamber. The swirler has a total height of $H = 30$ mm. The swirl number, defined as the ratio between the axial flux of tangential momentum and the axial momentum flux, has been estimated from the device geometrical properties. By assuming solid body rotation flow within the device, uniform axial velocity and negligible pressure effects [23], the corresponding geometrical swirl number is:

$$S_g = \frac{lD}{nd^2}\left[1 - \left(\frac{D_b}{D}\right)^2\right] \approx 0.4, \tag{1}$$

where l is the offset distance of the inlet orifice, relative to the main axis, D is the swirler outer diameter, n is the number of orifices, d is the orifice diameter, and D_b is the diameter of the inverted cone base. For the studied swirler SW06I, $l = 3.85$ mm, $D = 10$ mm, $n = 6$, $d = 2.3$ mm and $D_b = 8$ mm.

2.2 Numerical model description

All numerical results presented in this work have been carried out with a code from ANSYS (Fluent). This is motivated by a partnership with ANSYS/France in the framework of the Magister Consortium [10]. The physical and chemical models used in this work are directly chosen from this code available choices.

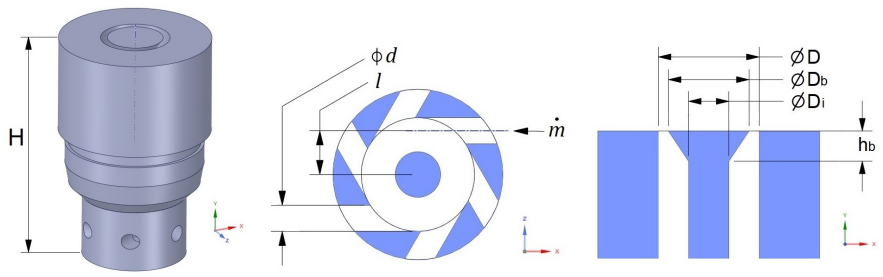

(a) SW06I. (b) Inlet section. (b) Outlet section.

Fig. 2 Combustion chamber schematic view. In the experimental configuration: 1 swirler, 2 cooling base, 3 confinement, 4 quartz window, adapted from [26].

For the sake of brevity, efforts of validation, in terms of the solution procedure, have not been made in this work.

In all studied cases, the balance equations of momentum and mass have been solved together with turbulence and combustion models. The functions and particularities of each model are briefly discussed and their primary sources are referenced, where they have been derived and presented with a more detailed description.

2.2.1 Turbulence modelling

The turbulence closure problem in this work is solved using Reynolds-Averaged Navier-Stokes (RANS) equations, due to their reasonable computational cost [17]. In the derivation of the $k-\epsilon$ model, it is assumed that the flow is fully turbulent and the effects of molecular viscosity are negligible. The first transported property is the turbulent kinetic energy, k, which describes the energy associated to the turbulent fluid motion. The second one is commonly referred to as the turbulent dissipation rate, ϵ, which determines the small scales of the turbulence. The third important specification in the $k-\epsilon$ model is the turbulent viscosity, which is modelled as a function of these transported flow properties using the Boussinesq hypothesis [18]:

$$\nu_t = C_\mu \frac{k^2}{\epsilon}, \tag{2}$$

where C_μ is a model parameter.

A variation from the standard $k-\epsilon$ is used in this work, i.e., the realizable $k-\epsilon$ model. The standard two-equation model is known to be over-predictive for the eddy viscosity in cases of flows with a high mean shear rate, due to its turbulent viscosity formulation. A new formulation for the model parameter C_μ ensures mathematical realizability, involving the effect of mean rotation on turbulence stresses, and avoiding negative normal stresses in cases of large

mean strain rates. This model also incorporates a new dissipation rate equation, based on the dynamic equation for fluctuating vorticity. It has been shown to predict more accurately the behaviour of flows involving rotation [32].

2.2.2 Premixed combustion modelling

The combustor studied in this work belongs to the group of premixed combustion devices. A perfectly homogeneous methane and air mixture is thus assumed to enter the computational domain, with a known fuel/air equivalence ratio. The premixed combustion model used here involves the solution of a transport equation for the reaction progress variable [37]. The instantaneous progress variable c is a binary entity, where $c = 0$ denotes fresh gases and $c = 1$ denotes burnt gases [5]. The progress variable is usually interpreted as a normalized temperature:

$$c = \frac{T - T_u}{T_b - T_u}. \tag{3}$$

The usual additional assumptions for the numerical model formulation simplification are: perfect gases, incompressible flow, constant heat capacities and unity Lewis numbers. This model has been derived to describe a flame in the wrinkled flamelets region, discussed in the results section.

The unclosed transport equation of the Favre-averaged progress variable, $\tilde{c}$, has the form:

$$\frac{\partial}{\partial t}\left(\bar{\rho}\tilde{c}\right) + \frac{\partial}{\partial x_i}\left(\bar{\rho}\tilde{u}_i\tilde{c}\right) = \frac{\partial}{\partial x_i}\left(\bar{\rho}\,\frac{\nu_t}{Sc_c}\frac{\partial \tilde{c}}{\partial x_i}\right) + \bar{\dot{w}}_c. \tag{4}$$

Both time-based (Reynolds) and density-based (Favre) averages have been used, denoted as $(\bar{\cdots})$ and $(\tilde{\cdots})$, respectively [28]. The first term on the RHS of the equation is a closure of turbulent scalar fluxes, known as the gradient assumption, and it is often used in turbulent combustion models [11], even if it may be of questionable validity for flames with large expansion ratios between the fresh and burnt gases [4]. The turbulent Schmidt number defines the ratio of the turbulent transport of momentum and the turbulent transport of mass and it is assumed to have a constant value of $Sc_c = 0.7$ [36].

The average chemical source term, $\bar{\dot{w}}_c$, is modelled here as function of the flame surface density, which accounts for the strain and stretch of the flame surface due to turbulence. The mean reaction rate is modelled as [7]:

$$\bar{\dot{w}}_c = \rho_u U_l \Sigma, \tag{5}$$

where ρ_u is the density of the unburnt mixture, and U_l is the laminar flame velocity, a property of premixed air/fuel mixtures.

The equation for the transport of the net flame surface area per unit volume Σ may be written as:

$$\frac{\partial}{\partial t}(\Sigma) + \frac{\partial}{\partial x_i}(\tilde{u_i}\Sigma) = \frac{\partial}{\partial x_i}\left(\frac{\nu_t}{Sc_c}\frac{\partial \Sigma}{\partial x_i}\right) + \kappa_t \Sigma - D, \tag{6}$$

where κ_t and D are unclosed terms which require, therefore, modelling. The turbulent strain rate, κ_t, is related to the stretch rate of the flame due to the turbulence motions and it is fitted from DNS data, and D is a destruction term required to avoid the infinite growth of the flame surface area [27].

2.3 Mesh generation, boundary conditions and numerical schemes

The computational grid has been generated using the software *Fluent Meshing* from *Ansys*. A three-dimensional mesh is generated from the computational domain described in the previous section. All meshings in this work consist of unstructured polyhedral elements.

A mesh sizing study is performed at the swirler region, in an isothermal flow study presented in section 3.1. Three distinct meshings of the swirler region are studied: a rough (mesh a), a medium (mesh b), and a fine mesh (mesh c), consisting of 270 thousand, 2 million and 3.8 million elements, respectively. The average cell size of each meshing system is $\Delta = 0.3$ mm, $\Delta = 0.13$ mm and $\Delta = 0.10$ mm, respectively. No mesh sizing study is performed within the combustion chamber, due to the scarceness of the available computational resources. The mesh refinement at this region is thus limited by these resources.

For the reactive flow study, presented in section 3.2, the computational grid is refined at the swirler's surface and lower combustion chamber regions (average cell sizing $\Delta_I = 0.10$ mm and $\Delta_{II} = 0.23$ mm, respectively), where larger gradients of velocity, turbulence and combustion properties are expected to occur. A single element is placed normal to the wall surfaces throughout the domain, with length of $\Delta = 0.035$ mm on the smallest cells, which are located around the inverted cone base. The mesh sizing is larger inside the swirler and at the upper part of the combustion chamber, which average cell sizings of $\Delta_{III} = 0.30$ mm and $\Delta_{IV} = 1.00$ mm, respectively.

The six inlets at the base of the swirler are set as pressure inlet boundary conditions (BC). A fixed absolute pressure of $P_{in} = 101$ kPa is set in all inlet surfaces, illustrated in Fig. 2. The outlet is the reduced area at the top of the combustion chamber, resulted from the usage of the pyramid-shaped structure, depicted in Fig. 1. This area has been designed to equal the total surface area of the six inlet surfaces, which is a technique for avoiding the occurrence of reverse flow at the outlet boundaries. A constant mass flow rate BC is set at the outlet surface, directed outwards, relative to the computational domain. All walls have no slip and adiabatic conditions, i.e., zero heat exchange with the exterior, unless otherwise stated. All turbulence models use standard wall functions for near-wall treatment.

The pressure-based coupled algorithm is used for pressure-velocity coupling. Spatial discretization for momentum, progress variable and flame area

density balance equations use the second-order upwind scheme. For the turbulent kinetic energy and turbulent dissipation rate equation, the first-order upwind scheme is used. Both steady and transient RANS are used in this work. All relaxation factors are set as default, according to Ansys Fluent 2019 R1. The first-order implicit scheme is used for the transient formulation, with a time-step of $\Delta t = 20$ μs, which respects the limits for the cell convective Courant number.

3 Results and Discussion

In this section, the obtained numerical results are presented and discussed. First, the numerical swirl number is determined and used as a comparison metric for meshing and boundary conditions at the swirler walls. Comparisons with the geometrical swirl number presented in section 2.1 are also drawn. The reactive results are then presented, and the corresponding flow field properties are analyzed for different methane/air equivalence ratios, and, thus, for different flame regimes.

3.1 Isothermal flow study: swirl number determination

The isothermal studies in this section are performed using the whole computational domain, i.e., the swirler and combustion chamber. The fluid mixture properties are assumed constant: $\rho = 1.225$ kg/m^3 and $\mu = 1.79 \cdot 10^{-5}$ kg/m.s for density and dynamic viscosity, respectively. The total mass flow rate through the six combined inlet orifices is $\dot{m} = 0.001715$ kg/s, which corresponds to a volumetric flow rate of $\dot{\forall} = 1400$ cm^3/s, chosen to represent the higher values experimentally studied [23]. Note that velocity measurements are not available for validation purposes.

The numerical swirl number is calculated at the swirler exit surface, i.e., adjacent to the combustion chamber base. Using the turbulence model and boundary conditions described in section 2, a mesh study is performed, considering the three swirler meshings discussed in section 2.3. The calculated numerical swirl number for the three meshing cases is $S_a = 0.83$, $S_b = 0.75$ and $S_c = 0.72$, respectively. Thus, the swirl number seems to converge to a value of $S \approx 0.7$, though a difference of less than 5 % is perceptible from cases b to c, indicating mesh b independency.

In order to allow for a more detailed comparison between the three meshing cases, the flow field within the swirler is now analysed. The swirling motion inside the swirler is represented in Fig. 3. The contours of the the z axis component of the flow velocity, which is the direction perpendicular to the evidenced section, indicate a counter-clockwise rotation inside this device. A good symmetry between both sides may be perceived in all three cases. It is also possible verify that the solution of mesh a seems to result in an over-smoothing of the flow features as compared to cases b and c. Qualitatively,

very similar results from cases b and c may also be perceived, except for a slightly more symmetrical flow in the finer mesh case. This suggests, again, that mesh independency within the swirler has been achieved for cases b and c.

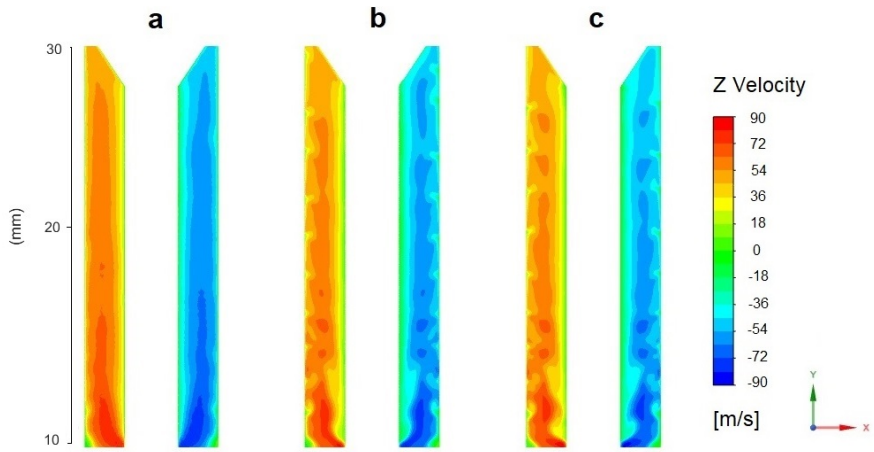

Fig. 3 Contours of z velocity component at the planar section of the swirler, from inlet (bottom) to outlet (top) for 3 different cases of mesh refinement (meshings a, b and c.

Further comparisons involving the vertical velocity component, in the direction of the y axis, may be seen in Fig. 4. Attention is drawn to the top part of the same swirler section as previously analysed, where a flow velocity increase occurs due to the presence of the bluff body. Two cases are directly compared: no-slip boundary condition and zero shear stress condition at the inner and outer walls of the swirler. The purpose of this comparison is to assess the need to describe the boundary layer flow in such a swirler configuration. In both cases, a central recirculation zone (CRZ) may be perceived at the internal part of the annular section. The presence of this CRZ is unexpected and has not been addressed by the associated experimental works [[26], [23]]. Apparently, due to the occurrence of a vigorous swirling motion, the centrifugal effect dominates over other effects, and the centrifugal force drives the fluid outward to the sidewalls and creates an axisymmetric column-like cavity along the axis [35]. Since the effects of viscous dissipation at the walls are not present in the case of zero shear stress, it may be inferred that the occurrence of such recirculation is not of a viscous nature, but of a pressure gradient related force. As an outcome of the present analysis, attention should be drawn to the swirler geometry, in particular to the bluff body cone angle, in order to avoid a CRZ. Such CRZ may indeed enhance the possibility of observing a flame flashback into the swirler, which could severely damage the combustion system [16].

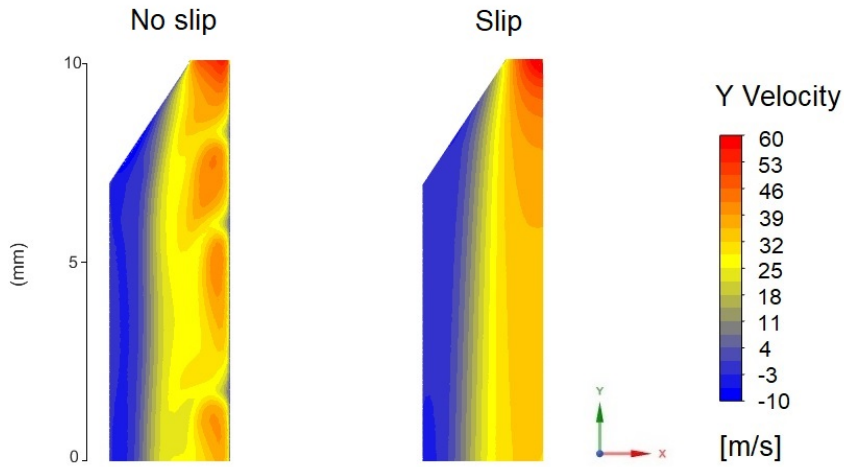

Fig. 4 Contours of y velocity component at the planar section of the swirler, with detail on top (exit) part. Two types of boundary conditions are compared: no slip walls (left) and walls with zero shear stress (right).

An analysis of the flow structure at the swirler exit surface is now presented, for cases of no slip and zero shear stress walls. Contours of axial velocity, v_y, and tangential velocity, v_θ, are displayed in Fig. 5, at the swirler annular exit surface, and the averaged circumferential values as a function of the surface radius are given in Fig. 6. As it may be seen in Fig. 5, the velocity components distribution is non-uniform for all cases. Cases of slip walls results are characterized by a circumferential symmetry, which is not observed for no slip cases. Indeed, along the tangential direction v_y and v_θ exhibit, for no slip wall case, important non-uniformities which could be related to a reminiscence of the swirler orifices fluid passage. Investigating further this point has not been attempted. Note, also, that such non-uniformities could lead to unstable fluid motions, which are not captured by RANS simulations. Note, as it could be expected from mass conservation, that similar values of average axial velocity at the swirler exit ($\bar{v}_y \approx 49.5$ m/s) have been determined.

Further criticism on the assumptions used for determining the geometrical swirl number [Eq.(1)] may be exerted by examining the circumferentially averaged velocity components for cases no slip and slip walls, given in Fig. 6. Indeed, this figure allows to observe that, for the case of slip walls, the linear dependency of $\bar{v}_\theta$ with r was a reasonable assumption, but the uniform $\bar{v}_y$ hypothesis used is clearly inadequate to describe the computed flow field. Concerning now case of no slip walls, Fig. 6 results indicate that, within the bulk flow, $\bar{v}_y$ is a monotonically increasing function of r at the swirler exit, whereas $\bar{v}_\theta$ exhibits a non monotonic behaviour. Both these functional dependencies seem to invalidate the simplifying assumptions used to derive the geometrical swirl number [Eq.(1)] [23], of solid body rotation flow within the device, a

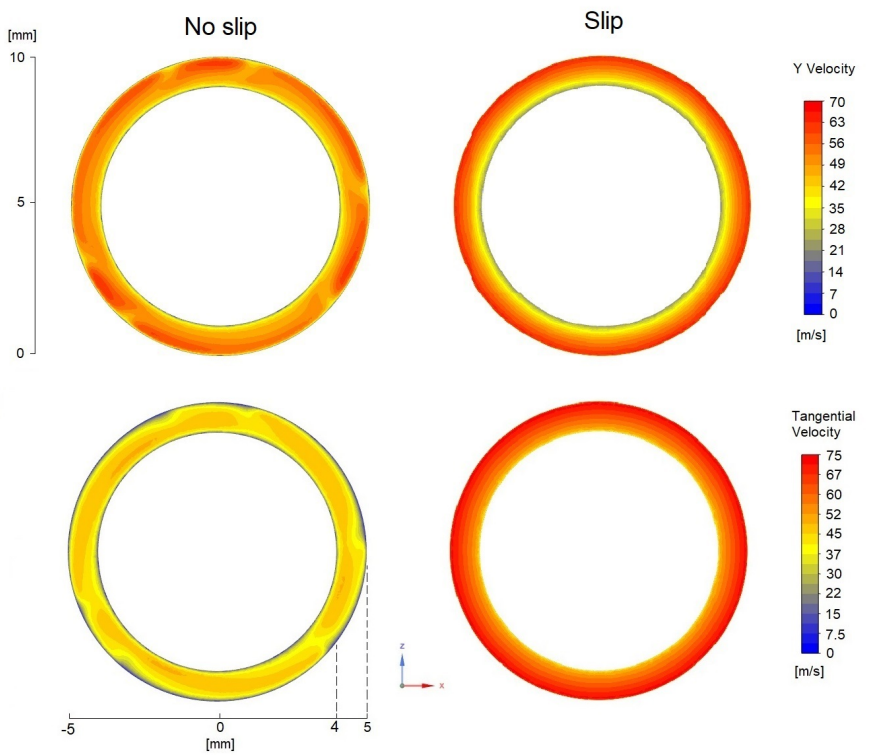

Fig. 5 Contours of y velocity component (top) and tangential velocity component (bottom) for cases of no slip and slip walls, at the swirler exit surface.

uniform axial velocity and negligible pressure effects. Indeed, the no slip walls results suggest that more adequate behaviours could be given by $\bar{v}_y \propto r$ and $\bar{v}_\theta \sim$ uniform.

3.2 Reactive flow study

The reactive flow results described in this section have been carried out with the realizable $k-\epsilon$ turbulence model. Since no experimental data is available for these flow properties, it is impossible to determine the most adequate turbulence model for this studied system by examining the obtained results only. The realizable $k-\epsilon$ is, then, chosen, as it has been pointed out in the literature as the most predictive two-equation model for high swirling flows, with the best agreement with experimental results [22]. The premixed combustion Extended Coherent Flamelet Model is applied to obtain all results, described in section 2.2. The unburnt fluid mixture properties, such as in the isothermal studies of the previous section, are $\rho = 1.225$ kg/m^3 and $\mu = 1.79 \cdot 10^{-5}$ kg/m·s for density of fresh gases and dynamic viscosity, respectively. The temperature of the unburnt gases is $T_u = 300$ K. The same total mass flow rate from the

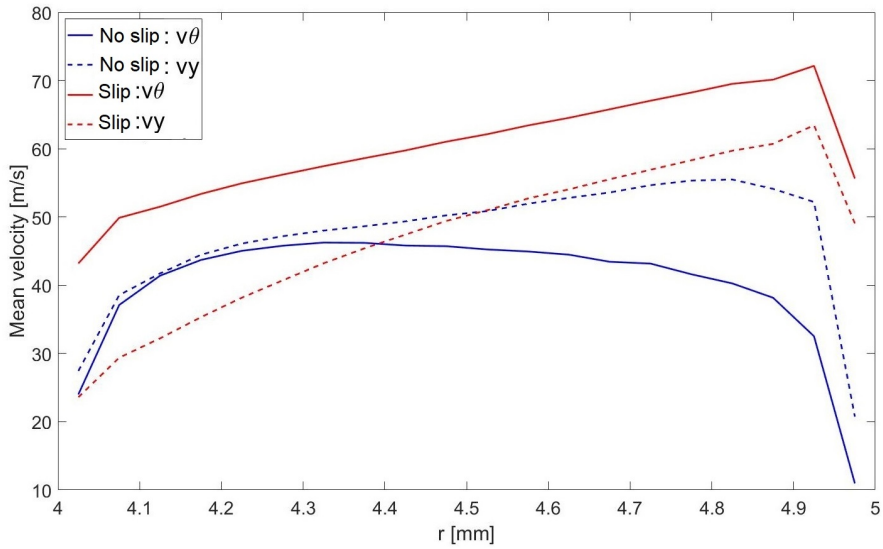

Fig. 6 Circumferentially averaged values of y velocity component (dashed lines) and tangential velocity component (solid lines) at the exit surface, for cases of no slip and slip walls.

isothermal studies is used, also: $\dot{m} = 0.001715$ kg/s, which corresponds to a volumetric flow rate of $\dot{\forall} = 1400$ cm^3/s. Boundary conditions follow the procedure described in the preceding section. The pressure-based coupled algorithm is again used for pressure-velocity coupling.

Two flame topologies are numerically defined and characterized in this section: flame regimes IV (outer recirculation zone flame) and II (unstable flame) [[26], [23], [31]]. The equivalence ratio values of the numerically obtained flame topologies do not directly correspond to their experimental counterparts. Indeed, the values of ϕ used in the computations are $\phi = 0.83$ and $\phi = 0.70$ for regimes IV and II, respectively, whereas the corresponding experimental values are $\phi = 0.73$ and $\phi = 0.62$. Further decreasing of the equivalence ratio below $\phi = 0.70$ has led to numerical instability, and a consequential flame blow-off. This is possibly due to insufficient mesh sizing at the upper part of the combustion chamber, since leaner flames tend to be longer and detach from the combustion chamber base. The shorter combustion chamber used in this study ($H_c = 100$ mm), with respect to its experimental counterpart ($H_c = 170$ mm), may also hinder the numerical convergence of this longer flame.

For the methane/air equivalence ratio of $\phi = 0.83$, used for defining flame topology IV, the values of adiabatic combustion temperature and laminar flame velocity [applied in Eq. (5)] are $T_b = 2000$ K and $U_l = 30.0$ cm/s, respectively. Since at this equivalence ratio the flame exhibited stability during the converging process, the steady RANS approach has been adopted. In order

to numerically obtain flame topology II, the methane/air equivalence ratio of $\phi = 0.70$ corresponds to values of adiabatic combustion temperature and laminar flame velocity of $T_b = 1840$ K and $U_l = 20.0$ cm/s, respectively. Due to the expected unsteady behaviour of this flame, transient (unsteady) RANS has been employed. Notice that RANS equations are not expected to fully predict the turbulent combustion instability nature, but could yield an overall indication of the instability onset. Most of the recent studies of thermoacoustic instabilities do indeed employ Large Eddy Simulations, as briefly discussed in section 1.

3.2.1 Overall flow structure

A three-dimensional representation of the recirculation zones present within the combustion chamber may be seen in Fig. 7, for a flow in the absence of chemical reaction and for the two flame topologies numerically studied in this work. Using iso-surfaces of $v_y = 0$, it is possible to observe the region within which the flow is redirected towards the combustion chamber base. This figure also shows the streamlines, which allow to infer the fluid motion. The outer recirculation zones (ORZ) may be identified at the corners of the chamber, through recirculating streamlines inside the $v_y = 0$ surface at these corners. The inner recirculation zone (IRZ) may be seen around the computational domain center axis, and it is associated to a bubble-shaped surface of $v_y = 0$ and to the streamlines that outline this bubble and penetrate its top region. The main swirling methane/air jet may be seen between the ORZ and IRZ, at the lower part of the combustion chamber. This jet expands downstream to the swirler exit, and interacts with the chamber walls. The upper recirculation bubble, noticeable in the isothermal case, is closed. Both flame regimes yield rather similar qualitative results, in terms of recirculation bubbles location.

The flow field within the combustion chamber is now analyzed in Fig. 8, in terms of the vertical velocity component (v_y) contours for an isothermal flow and the two flame regimes numerically studied in this work. This planar section is the same as depicted in Fig. 3. The recirculation zones, which are commonly observable in such swirling systems, may be precisely identified in that figure. These zones are materialized in by the streamlines that indicate the fluid redirection towards the bottom of the combustion chamber, and play an important role in the flame stabilization. They are associated mainly due to the fluid sudden expansion from the swirler to the combustion chamber, and also to the swirling motion. Two different recirculation regions may be observed here: the outer recirculation zone (ORZ) and the inner recirculation zone (IRZ). The outer recirculation zone occurs at the bottom corners of the combustion chamber, at $-20 < x < -1$ mm and $0 < y < 15$ mm, approximately, whereas the inner recirculation zone is located at the center of the combustion chamber, at $-10 < x < 10$ mm and $10 < y < 40$ mm. Confirming the discussion developed in the light of Fig. 7, it is possible to observe the swirling jet expansion upon exiting the swirler, in the region between the ORZ and IRZ. This jet impacts the combustor walls and is deflected upwards

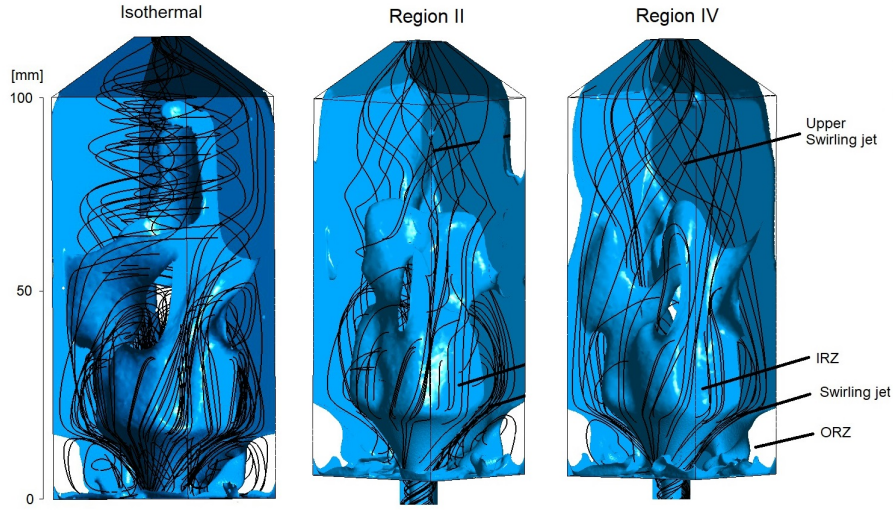

Fig. 7 Representation of recirculation bubbles, through iso-surfaces of $v_y = 0$ m/s (blue), with superimposed streamlines from the swirler exit (black), for the studied isothermal and reactive cases.

and downwards. The velocity field is higher in magnitude at flame region IV. This is due to the higher thermal expansion of chemical reaction heat release of this richer flame ($\phi = 0.83$).

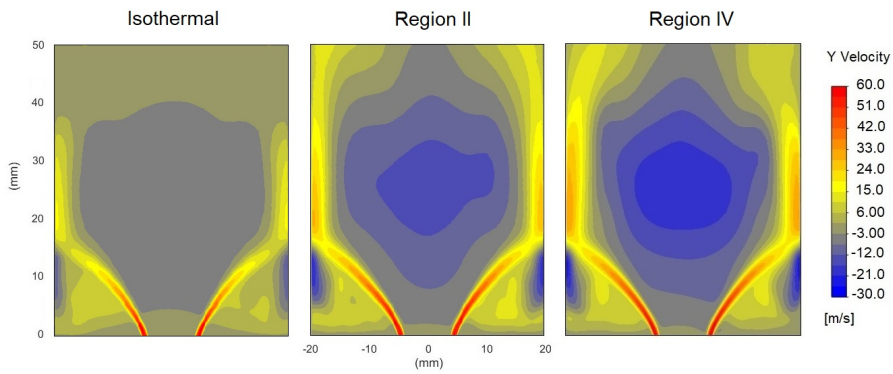

Fig. 8 Contours of y velocity component at the planar section of the lower combustion chamber region for the studied isothermal and reactive cases.

The turbulent viscosity ratio, with a color scale emphasis at the ORZ and swirling jet regions, is also compared in Fig. 9 for the three cases. This property ratio is proportional to a turbulent Reynolds number, which is a parameter that directly controls the turbulent combustion regime [25]. The values of this property suggest that the flow turbulence in the ORZ is such

that $\mu_t/\mu \approx 50$ for the isothermal case and $\mu_t/\mu \approx 20$ for topology II and $\mu_t/\mu \approx 10$ for topology IV. This occurrence could have been expected, as the mixture molecular viscosity increases as the temperature increases.

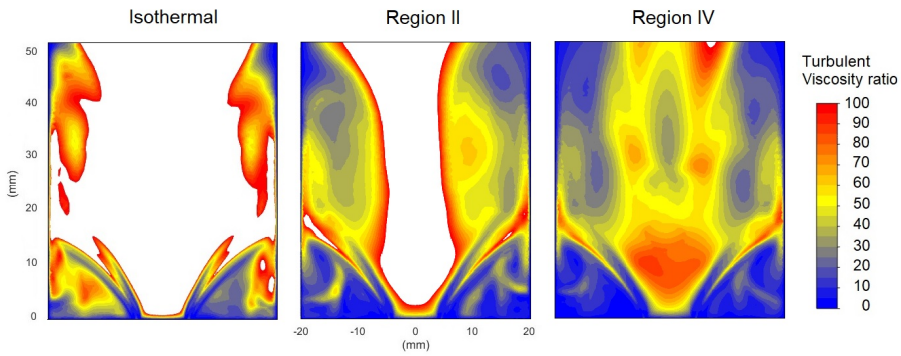

Fig. 9 Contours of turbulent viscosity ratio at the planar section of the lower combustion chamber region for the studied isothermal and reactive cases.

In order to corroborate this last assessment, the temperature field within the combustion chamber is now analysed for the two studied flame regimes in Fig. 10, with a color scale emphasis at the outer recirculation zone. As it may be seen, a recirculation of hot gases, at $T \approx 1300$ K for flame regime IV, occurs in this region, which is the main characteristic of the ORZ flame [31]. The mean temperature at the ORZ for flame regime II is $T \approx 700$ K, which represents a rather low concentration of burnt gases at this region. From Figs. 8 and 10, a flow of high velocity magnitude ($v_y \approx 30$ m/s for flame topology IV) of hot gases adjacent to the chamber walls may be identified also. It could be inferred that the used assumption of zero heat flux at the walls boundary may lead to an under-prediction of the heat flux near the walls and, therefore, to an incorrect temperature distribution.

These color maps have been chosen specifically to highlight the depicted properties distributions in regions of the flow field that are relevant to the combustion stabilization. The regions of interest for turbulent viscosity ratio is at the outer recirculation zones and around the swirling jet and for temperature field is at the outer recirculation zone and at the wall vicinity. The presented analysis of the turbulent viscosity ratio allows verification of the turbulence intensity levels at a region of comparatively low turbulence levels, due to fluid stagnation and recirculation. The analysis of this temperature range at the wall vicinity yields an insight on the possible effects of wall heat fluxes in the system. Additionally, the temperature fields at the outer recirculation zones should provide an insight on the variation of turbulent viscosity ratio for different flame regimes. The flow regions corresponding to the burned gases are, here, considered to be of lesser importance, and thus are not discussed.

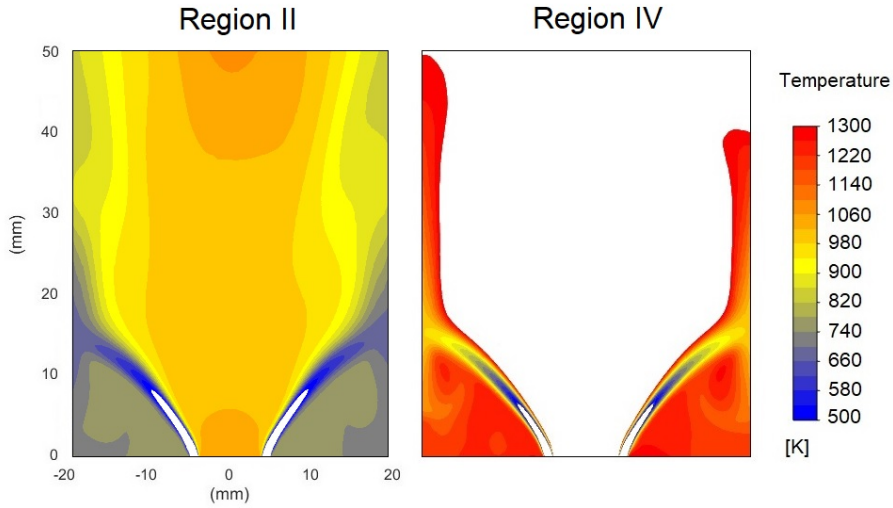

Fig. 10 Temperature field at the planar section of the lower combustion chamber region for the studied reactive cases.

For the sake of gaining further insight on the reactive flow properties, Fig. 11 depicts the flame surface density, Σ, distribution, computed by solving Eq.(6). Examining this figure allows to observe that the flame surface lies around the fuel/air swirling jet and, again, exhibits a strong interaction with the wall. The smaller value of U_l for the leaner combustion regime (flame topology II) leads to a smaller value of Σ, which then leads to a smaller prediction of the flame surface density.

The two turbulent and combustion properties previously analyzed are quantitatively compared in Fig. 12, for flame regimes 2 and 4. The turbulent viscosity ratio and flame surface density are depicted at a height of $y = 10$ mm, i.e., crossing the outer recirculation zones and the expanding, swirling jet, at the same plane represented in Fig. 8. The values of the turbulent viscosity ratio at the ORZ for regime 2 are approximately 14 % higher in average than regime 4, as it has been explained due temperature differences. At the IRZ, where concentration of burnt gases is shown to be higher, the increase is more significant: 60 % higher for flame regime 2. The comparison between values of flame surface density at this same region shows an increase of over 100 %, as previously discussed at the qualitative comparison given in Figs. 9 and 11.

3.2.2 Flame regime IV - Outer Recirculation Zone flame

The flame regime studied in this section is known as flame regime IV, defined and characterized experimentally in the literature [[26], [23], [31]]. As it has been underscored above, at the highest equivalence ratio experimentally studied, $\phi = 0.73$, the average flame brush is located around the swirling,

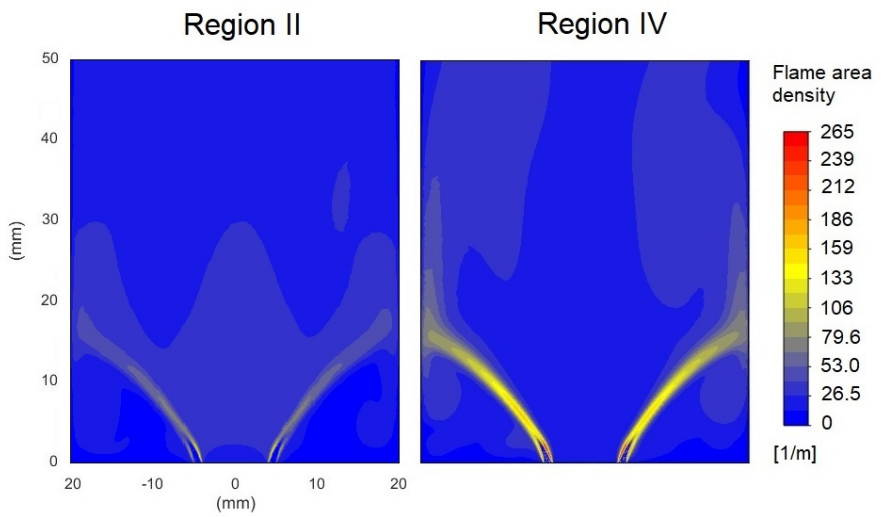

Fig. 11 Flame surface density (Σ) at the planar section of the lower combustion chamber region for the studied reactive cases.

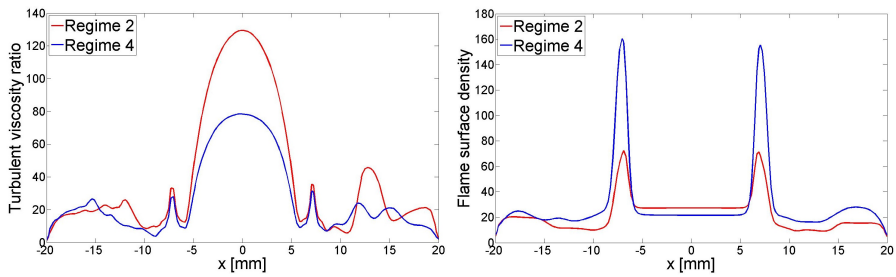

Fig. 12 Turbulent viscosity ratio (left) and flame surface density (right) at a height of $y = 10$ mm from the combustion chamber base, for flame regimes 2 and 4.

expanding jet and at the outer recirculation zones, i.e., at the vicinity of the combustion chamber corners.

In order to gain further insight of this flame topology, a comparison between numerical and experimental results for a representation of the average flame brush is given in Fig. 13. The experimental instantaneous PLIF-OH signal has been binarized, assuming a zero value when OH is absent, and one when OH is present [23]. As a consequence, the binarized results should represent a progress variable, where $c = 0$ denotes fresh gases and $c = 1$ denotes burnt gases, obtained from Eq.(4). The average value of this property should, then, represent the mean flame surface.

As it can be seen from Fig. 13, the computed progress variable field predicts the average flame around the expanding jet and outer recirculation zones. In the ORZ, the mean progress variable value is $c \approx 0.5$, and downstream to the swirling jet $c \approx 0.8$. The flame expands and starts to interact with the

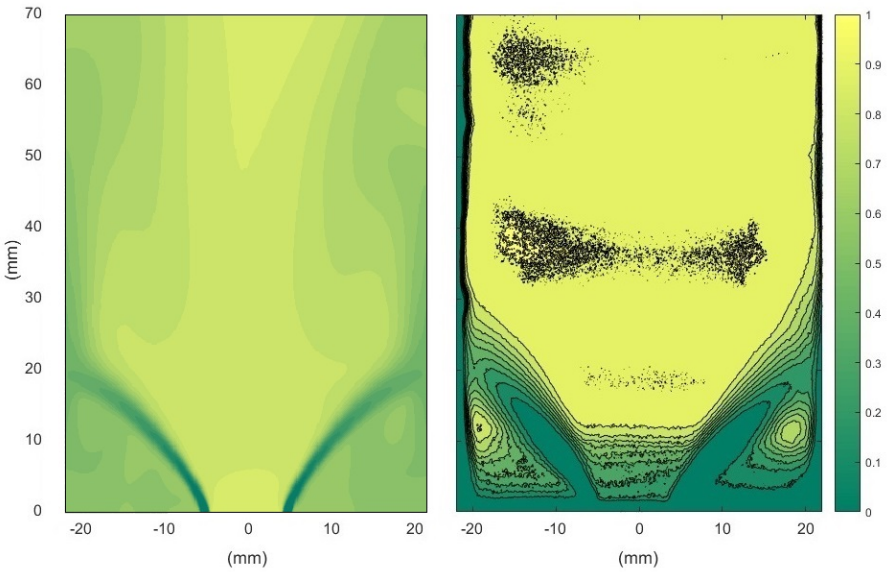

Fig. 13 Flame regime IV: contours of computed progress variable (left) and average OH radical binarized image, measured with PLIF (right), adapted from [23].

combustion chamber walls at similar positions, $y \approx 15$ mm, from the chamber base. The agreement between the model and the experiments is qualitative. A discrepancy exists, in particular, concerning the average flame brush thickness obtained experimentally ($\delta \approx 3$ mm) which may be seen to be larger than the computed counterpart ($\delta \approx 1$ mm). This quantity is estimated as being the distance between fresh gases and burnt gases, normal to the flame front. Nevertheless, the overall position of this flame front is adequately predicted. The obtained discrepancies could be due to the above mentioned computational model shortcomings.

A more in-depth comparison between numerical and experimental studies is presented in Fig. 14. In this figure, at the same plane represented in Fig. 13, for three distinct heights from the combustion chamber base, a quantitative evaluation of the progress variable is given. This figure allows to observe that, at the lowermost comparison position, i.e., 10 mm, the computed position of the minimum progress variable value is similar to the experiments, and is found to lie at $x \approx 12$ mm. However, the computed results indicate a larger minimum progress variable, 0.22, value than the measured ones, 0.05. Furthermore, at this same height, the experiments suggest the presence of burned gases (progress variable $c \approx 0.95$) at the combustor center ($x \approx 0$ mm), whereas the computed results value is 0.8. Further downstream, at 20 and 30 mm height, the discrepancy between the numerical results and experimental data are larger, even if the overall transversal progress variable distribution is rather uniform. The experiments indicate that these regions correspond mostly to

fully burned gases (unity progress variable value, whereas the computed flame is found to be longer, since the progress value is of the order of 0.8 at both heights. These quantitative discrepancies could be an artifact of the different progress variable definitions. Indeed, the computations use a model equation for the transport of this average property, which is deemed to represent a normalized temperature or limiting reacting species. However, in the experiments a progress variable was defined based on the OH radical laser induced florescence signal, which is absent in the fresh unburned gases and present at the burned, equilibrium, state. These different definitions could be at the root of the observed quantitative discrepancy.

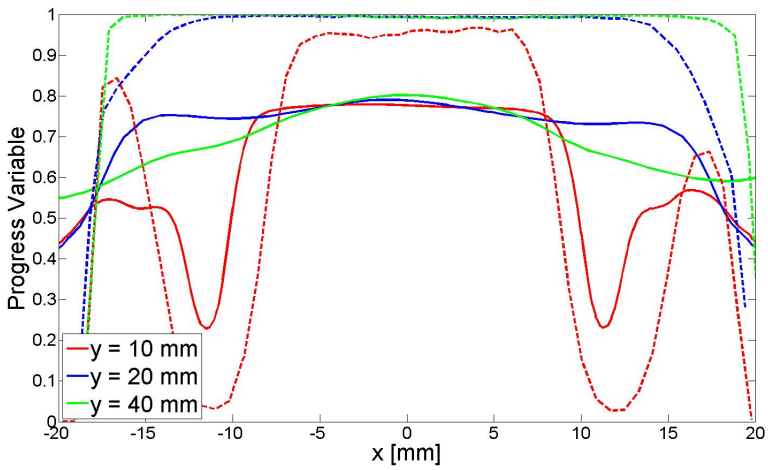

Fig. 14 Comparison of the combustion progress variable at three distinct heights from the combustion chamber base: $y = 10, 20$ and 40 mm. Solid lines: numerical solution; dashed lines: experimental data [23].

3.2.3 Flame regime II - Unstable flame

The flame regime addressed in this section is known as flame II [[26], [23], [31]]. As the equivalence ratio decreases, this flame regime occurs in the transition between stable regimes III (V-Flame) and I (Tornado Flame). The flame brush location is unstable, as it pulses between the upper swirling jet and the inner recirculation zone, thus resembling the flame regimes I and III intermittently. The computed flame is found to oscillate between the inner recirculation zone and the upper swirling jet, intermittently detaching from the combustion chamber base. These unsteady results are not shown here for the sake of brevity.

The obtained average flame topology is now compared with the experimental results in Fig. 15. A total of 200 instantaneous images from the unsteady

RANS simulation, within a time lapse of $\Delta t = 60$ ms have been averaged, in order to obtain a representation of the flame brush location. As a consequence of the intermittent behaviour, two local maximum values of the progress variable may be observed at the domain center: at the IRZ ($c \approx 0.6$), between the expanding jets and at the upper swirling jet, near the domain exit. Experimentally, the peak value of the binarized, averaged OH fluorescence is $c \approx 0.8$. A small amount of burnt gases is perceived at the ORZ at the computed progress variable ($c \approx 0.2$), whereas no OH is experimentally registered at the ORZ. Such as in the flame regime IV, the average flame brush thickness obtained experimentally ($\delta \approx 3$ mm) seems to be larger than the computed counterpart ($\delta \approx 2$ mm). Nevertheless, the qualitative agreement of modeled and experimental results is remarkable.

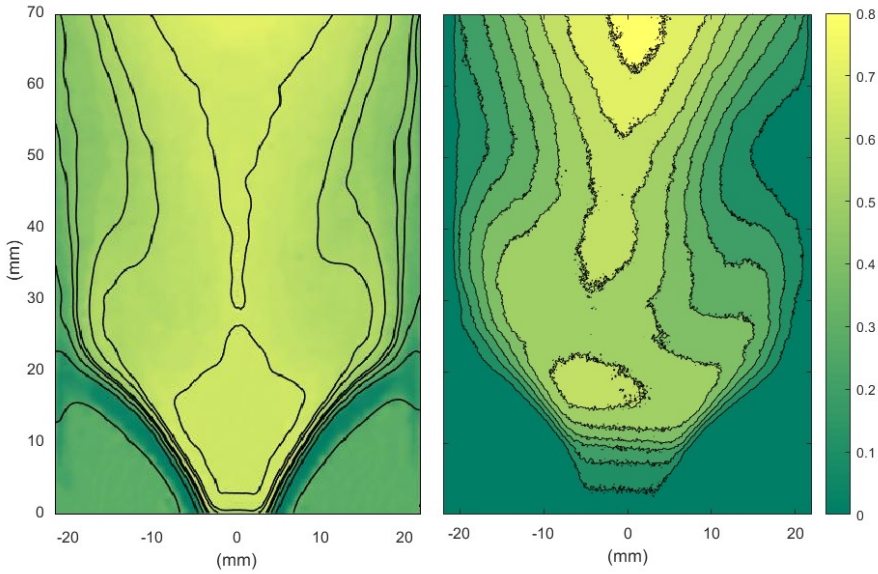

Fig. 15 Flame regime II: contours of computed progress variable (left) and average OH radical binarized image, measured with PLIF (right), adapted from [23].

3.2.4 Borghi diagram analysis

The Borghi diagram is a classical [25] representation of turbulent premixed flame regimes. This diagram compares the velocity and length scales of the turbulent motion and the combustion process, and allows to elaborate on the outcome of turbulence/flame interactions. Moreover, the role of the turbulent Reynolds number and of the Damköhler number are clearly evidenced. Also using this diagram, criticism may be exerted on the pertinence of turbulent combustion models, which is the aim pursued here.

An analysis of flames IV and II behaviour, with respect to the flame/turbulence interaction, is thus given in Fig. 16. The ellipses locations, which delimit the turbulent premixed flame regimes have been estimated from the computed turbulent Reynolds number and the ratio between the computed root-mean-square velocity fluctuation and the laminar flame velocity, u'/U_l. Notice that the turbulent Reynolds number estimated at this diagram is based on an order of magnitude analysis of the thermal flame thickness, which could differ significantly from the value computed using detailed chemistry and transport [13]. Figure 16 indicates that the studied flames could be situated in the thickened flamelet regime within the Borghi diagram, in which the smallest turbulent eddies would penetrate the flame and disturb the chemical reaction process. This turbulence/combustion interaction regime is expected to significantly depart from the laminar flame situation, for which the Coherent flamelet model [27] was envisaged. Therefore, it could be inferred that the studied turbulent premixed flame would not be suited for predictions using the coherent flame model applied here. However, determining with more precision the suitability of this model for predicting the studied flames would require the availability of more detailed experimental data, such as velocity measurements.

4 Conclusion and Perspectives

The numerical study of turbulent, premixed flames within a square-sectioned swirling combustion chamber has been performed in this work. This study aimed to model, using a Reynolds-Averaged Navier-Stokes approach, the lean premixed turbulent swirling combustor developed at PUC-Rio, in partnership with CentraleSupelec EM2C Laboratory. First, isothermal flow simulations have been performed with attention to the swirler region. Then, using a classical premixed combustion model, two distinct flame topologies [31] have been numerically characterized. Comparisons with experimental results have also been drawn.

The isothermal flow results have shed light upon the flow behaviour within the swirler, as well as the mesh refinement and boundary condition settings impacts on the numerical solution. The resulting swirl number has been shown to decrease when a finer mesh is used, converging to a value of $S \approx 0.7$, which is larger than the geometrical swirl number value, $S_g \approx 0.4$. The use of slip walls boundary conditions has yielded a significantly higher swirl number, and an over-simplified flow field. The comparisons of isothermal and reactive flow fields allowed to identify the impact of combustion on the flow field structure and turbulence properties. In particular, the chemical reaction heat release causes a flow acceleration, which closes the inner recirculation zone and limits its extension when compared to the isothermal flow.

The reactive flow results have shown that the obtained flame topologies agree qualitatively with their experimental counterparts. The two-equation, premixed combustion Extended Coherent Flamelet Model, coupled with the realizable $k - \epsilon$ turbulence model was able to predict the average behaviour

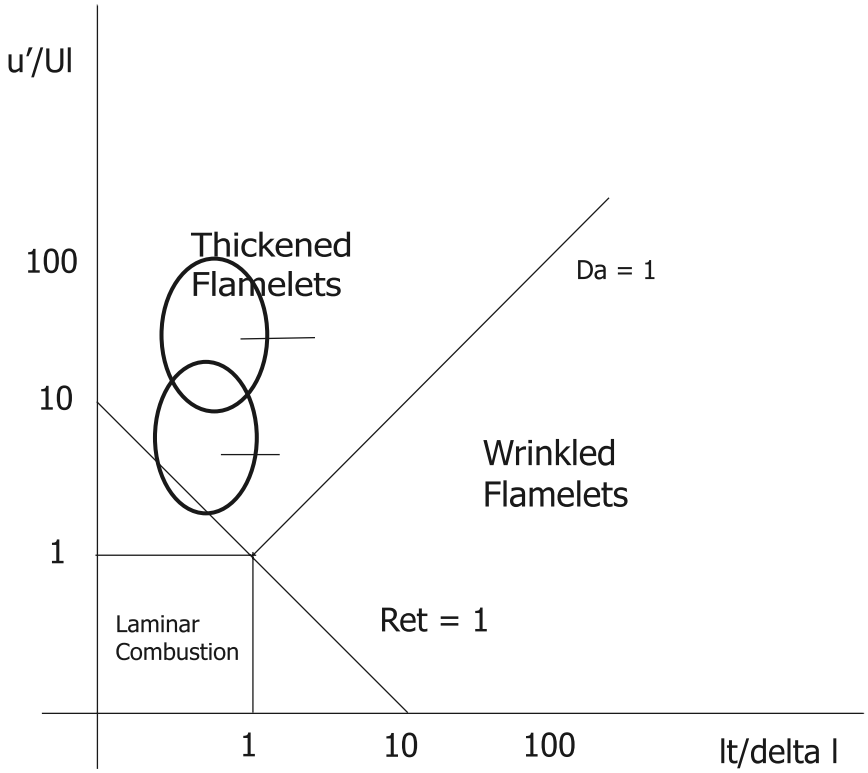

Fig. 16 Simplified Borghi diagram for turbulent premixed combustion. Adapted from [2]. The computed flame regimes locations at the diagram are given by the ellipses.

of flame topologies II and IV, observed experimentally [23], albeit at different equivalence ratio values.

In light of the obtained results, perspectives for future works include:

- The improvement of the mesh refinement at the swirler, which has been shown to impact the calculated swirl number and flow field within this device.
- The implementation of a taller combustion chamber ($H_c = 170$ mm), similar to that experimentally studied, as well as a refined mesh at its upper region. These modifications are of special interest when a leaner combustion topology is of interest, such as regime I. It has been observed experimentally that these flames are longer, and they have not been adequately reproduced with the adopted short combustion chamber.
- The investigation of the flame location at the Borghi diagram, discussed at section 3.2.4. Indeed, a more rigorous estimate of the flame thickness could change the location of the obtained flames at the diagram significantly. Nevertheless, the implementation of premixed combustion models

that are not limited by flame/turbulence interaction assumptions should be considered, such as PDF transport models [[12], [34], [8], [9], [1]].
- The effect of the implementation of finite wall heat fluxes on the resulting flow field and combustion properties. Indeed, the high velocity flow of hot gases adjacent to the combustion chamber walls suggests that heat fluxes may not be negligible, which has been demonstrated in experiments conducted elsewhere [14]. The assumption of adiabatic walls could be, therefore, improper.
- Full determination of combustion regime diagrams, i.e., as a function of equivalence ratio and volumetric flow rate, thus allowing to categorize the flame regimes stability and boundary limits, in accordance to the experimental studies [23].
- The application of Large Eddy Simulations, in order to improve the prediction of the unsteady behaviour and thermoacoustic instabilities, and also predict the coherent turbulent structures.

5 Acknowledgements

This study was financed in part by the Coordenação de Aperfeiçoamento de Pessoal de Nível Superior - Brasil (CAPES) - Finance Code 001 (Alain P. N. Coimbra). This work was performed while L. F. Figueira da Silva was on leave from Institut Pprime (CNRS, France). The authors gratefully acknowledge the support for the present research provided by Conselho Nacional de Desenvolvimento Científico e Tecnológico (CNPq, Brazil) under research grants no. 403904/2016-1. The authors are also grateful to Dr. Valéry Morgenthaler (Ansys/France) for the assistance and helpful comments on this work.

Conflict of Interest: The authors declare that they have no conflict of interest.

References

1. Andrade, F.O., Figueira da Silva, L.F., Mura, A.: Large eddy simulation of turbulent premixed combustion at moderate damkohler numbers stabilized in a high-speed flow. Combustion Science and Technology **183**, 645–664 (2011)
2. Ansys, I.: Extended coherent flamelet model theory. hrefhttp://www.afs.enea.it/project/neptunius/docs/fluent/html/th/node174.htm (2009). URL http://www.afs.enea.it/project/neptunius/docs/fluent/html/th/node174.htm. Access in: July 2019
3. Benard, P., Lartigue, G., Moureau, V., Mercier, R.: Large-eddy simulation of the lean-premixed preccinsta burner with wall heat loss. Proceedings of the Combustion Institute **37**, 5233–5243 (2019)
4. Borghi, R., Champion, M.: Modélisation et théorie des flammes, 1st edn. Editions TECHNIP (2000)
5. Bray, K.N.C., Libby, P.A., Moss, J.B.: Unified modeling approach for premixed turbulent combustion part I: General formulation. Combustion and Flame **61**, 87–102 (1985)

6. Caetano, N.C., Figueira da Silva, L.F.: A comparative experimental study of turbulent non premixed flames stabilized by a bluff-body burner. Experimental Thermal and Fluid Science **63**, 20–33 (2015)
7. Candel, S.M., Poinsot, T.J.: Flame stretch and the balance equation for the flame area. Combustion Science and Technology **70**, 1–15 (1990)
8. Celis Perez, C., Figueira da Silva, L.F.: Lagrangian mixing models for turbulent combustion: Review and prospects. Flow, Turbulence and Combustion **94**, 643–689 (2015)
9. Celis Perez, C., Figueira da Silva, L.F.: Study of mass consistency les/fdf techniques for chemically reacting flows. Combustion Theory and Modelling **1**, 465–494 (2015)
10. Consortium., M.: Magister consortium. https://www.utwente.nl/en/et/magister/AboutMagister/Consortium/ (2019). URL https://www.utwente.nl/en/et/magister/AboutMagister/Consortium/
11. Darabiha, N., Giovangigli, V., Trouvé, A., Candel, D.M., Esposito, E.: Coherent flame description of turbulent premixed ducted flames. Turbulent Reactive Flows **40**, 591–637 (1989)
12. Fox, R.O.: Computational models for turbulent reacting flows, 1st edn. Cambridge University Press, The Edinburgh Building, Cambridge CB2 2RU, UK (2003)
13. Grosseuvres, R., Comandini, A., Centaib, A., Chaumeix, N.: Combustion properties of $H_2/N_2/O_2$/steam mixtures. Proceedings of the Combustion Institute **37**, 1537–1546 (2019)
14. Guiberti, T., Durox, D., Scouflaire, P., Schuller, T.: Impact of heat loss and hydrogen enrichment on the shape of confined swirling flames. Proceedings of the Combustion Institute **35**, 1385–1392 (2015)
15. Guiberti, T.F., Durox, D., Zimmer, L., Schuller, T.: Analysis of topology transitions of swirl flames interacting with the combustor side wall. Combustion and Flame **162**, 4342–4357 (2015)
16. Huang, Y., Yang, V.: Dynamics and stability of lean-premixed swirl-stabilized combustion. Progress in Engergy and Combustion Science **35**, 293–364 (2009)
17. Inc., F.: Standard, RNG, and realizable k-ϵ models theory. hrefhttps://www.sharcnet.ca/Software/Fluent6/html/ug/node477.htm (2006). URL https://www.sharcnet.ca/Software/Fluent6/html/ug/node477.htm. Access in: July 2019
18. Jones, W.P., Launder, B.E.: The prediction of laminarization with a two-equation model of turbulence. International Journal of Heat and Mass Transfer **15**, 301–314 (1972)
19. Kraus, C., Selle, L., Poinsot, T.: Coupling heat transfer and large eddy simulation for combustion instability prediction in a swirl burner. Combustion and Flame **191**, 239–251 (2018)
20. Lourier, J.M., Stöhr, M., Noll, B., Werner, S., Fiolitakis, A.: Scale adaptive simulation of a thermoacoustic instability in a partially premixed lean swirl combustor. Combustion and Flame **183**, 343–357 (2017)
21. Ma, P.C., Wu, H., Labahn, J.W., Jaravel, T., IHME, M.: Analysis of transient blow-out dynamics in a swirl-stabilized combustor using large-eddy simulations. Proceedings of the Combustion Institute **37**, 5073–5082 (2019)
22. Mansouri, Z., Aouissi, M., Boushaki, T.: A numerical study of swirl effects on the flow and flame dynamics in a lean premixed combustor. International Journal of Heat and Technology **34**, 227–235 (2016)
23. Nobrega, G.S., Piton, L., Figueira da Silva, L.F., Scouflaire, P., Darabiha, N.: Experimental study of the effect of the swirl number on premixed combustion regimes and flame topologies. 11th Mediterranean Combustion Symposium pp. 1–12 (2019)
24. Noh, D., Karlis, E., Navarro-Martinez, S., Hardalupas, Y., Taylor, A.M.K.P., Fredrich, D., Jones, W.: Azimuthally-driven subharmonic thermoacoustic instabilities in a swirl-stabilised combustor. Proceedings of the Combustion Institute **37**, 5333–5341 (2019)
25. Peters, N.: Turbulent Combustion, 1st edn. Cambridge University Press. doi:10.1017/CBO9780511612701, The Edinburgh Building, Cambridge CB2 2RU, UK (2000)
26. Piton, L., Nobrega, G.S., Figueira da Silva, L.F., Scouflaire, P., Darabiha, N.: Experimental study of the influence of the swirl number on lean premixes combustion regimes. 17th Brazilian Congress of Thermal Sciences and Engineering pp. 1–9 (2018)
27. Poinsot, T., Veynante, D.: Theoretical and Numerical Combustion, 2nd edn. R. T. Edwards Inc., Philadelphia, PA 19118 USA (2005)

28. Pope, S.B.: Turbulent Flows, 1st edn. University of Cambridge, Edinburgh Building, Cambridge, CB2 2RU, UK (2000)
29. Rochette, B., Collin-Bastiani, F., Gicquel, L., Vermorel, O., Veynante, D.: Influence of chemical schemes, numerical method and dynamic turbulent combustion modeling on led of premixed turbulent flames. Combustion and Flame **191**, 417–430 (2018)
30. Scott Brewster, B., Cannon, S.M., Farmer, J.R., Meng, F.: Modelling of lean premixed combustion in stationary gas turbines. Progress in Energy and Combustion Science **25**, 353–385 (1999)
31. Shanbhogue, S.J., Sanusi, Y.S., Taamallah, S., Habib, M.A., Mokheimer, E.M.A.: Flame macrostructures, combustion instability and extinction strain scaling in swirl-stabilized premixed CH4/H2 combustion. Combustion and Flame **163**, 494–507 (2015)
32. Shih, T.H., Liou, W.W., Shabbir, A., Yang, Z., Zhu, J.: A new $k - \epsilon$ eddy viscosity model for high reynolds number turbulent flows. Computers Fluids **24**, 227–238 (1995)
33. Figueira da Silva, L.F., Mergulho, C.S., Piton, L., Scouflaire, P., Darabiha, N.: Experimental study of a lean premixed turbulent swirling flame stabilization. International Congress of Mechanical Engineering **24**, 1–9 (2017)
34. Vedovoto, J.M., Da Silveira Neto, A., Figueira da Silva, L.F., Mura, A.: Influence of synthetic inlet turbulence on the prediction of low mach number flows. Computers & Fluids **106**, 135–153 (2015)
35. Wang, Y., Yang, V.: Central recirculation zones and instability waves in internal swirling flows with an annular entry. Physics of Fluids **30**, 1–20 (2018)
36. Zimont, V., Polifke, W., Weisenstein, W.: An efficient computational model for premixed turbulent combustion at high reynolds numbers based on a turbulent flame speed closure. Journal of Engineering for Gas Turbines and Power **120**, 526–532 (1998)
37. Zimont, V.L.: Gas premixed combustion at high turbulence. turbulent flame closure combustion model. Experimental Thermal and Fluid Science **21**, 179–186 (2000)